

PSFC/JA-10-47

Pure-Bending Strain Investigations: Device and ITER Nb₃Sn Wires

Takayasu, M., Chiesa¹, L., Harris², D.L., Allegritti³, A., Minervini, J.V.

December 23 2010

**Plasma Science and Fusion Center
Massachusetts Institute of Technology
Cambridge MA 02139 USA**

¹Present address: Mechanical Engineering Department,
Tufts University, Medford, MA 02155, USA.

²Present address: Depth Enterprises LLC, Logan, UT, USA.

³Present address: JPMorgan, 125 London Wall, London, UK.

This work was supported by the U.S. Department of Energy, and the US ITER Project Office. A portion of this work was performed at the National High Magnetic Field Laboratory, Florida State University.

Abstract

This paper presents in detail recent pure-bending strain investigations of ITER Nb₃Sn wires including a pure-bending device development, bending effects on the critical currents and their model analyses. The pure-bending test device allows applying a uniform bending over a large range of bending strain on a strand sample under a large electromagnetic Lorentz force. Pure bending characteristics of five different Nb₃Sn wires including three internal-tin and two bronze wires were tested and evaluated with a newly developed integrated model that accounts for neutral axis shift, current transfer length, mechanical filament breakage and uniaxial strain release due to the applied bending load.

Keywords: Bending strain, pure bending, Nb₃Sn superconductor, critical current, neutral axis shift, current transfer, filament breakage.

Contents

1. Introduction
 2. Versatile robust pure-bending device
 - 2.1 Pure bending requirement
 - 2.2 Pure bending device
 3. Fabricated pure-bending test device for superconducting wire
 - 3.1 Gear driving
 - 3.2 Sample holder beam
 - 3.3 Effect of electromagnetic forces
 - 3.4 Finite element analysis
 4. Tested wires and critical current test conditions
 5. Test Results
 - 5.1 ITER TF pre-production Oxford and Luvata wires
 - 5.2 Other ITER-related wires
 - 5.2.1 EU EAS wire
 - 5.2.2 EM-LMI wire (ITER model coil wire)
 - 5.2.3 Furukawa wire (ITER model coil wire)
 6. Model analysis
 - 6.1 Critical current formula
 - 6.2 Conventional model of bending effects on strand critical current
 - 6.2.1 Perfect Current Transfer
 - 6.2.2 No Current Transfer
 - 6.3 Integrated model
 - 6.3.1 Neutral-axis shift effect
 - 6.3.2 Current transfer length effect
 - 6.3.3 Filament breakage effect
 - 6.3.4 Uniaxial strain release effect
 7. Discussion
 8. Conclusions
- Acknowledgements
- References

1. Introduction

Unexpected degradations of large Nb₃Sn superconducting conductor magnets, like ITER model coils, composed of more than 1000-strands have driven attention to bending effects of Nb₃Sn wires [1]-[6]. We have developed a variable bending device to characterize the critical currents of superconducting strands under pure bending [7]-[9] and have investigated pure-bending behaviors of various ITER Nb₃Sn wires [10, 11].

The pure-bending device was able to apply various uniform bending loads over a large range of strain up to 0.9% on a strand sample in liquid helium. The principal mechanism of the pure-bending device is similar to that developed by W. Goldacker, et al. for characterization of high temperature superconductors under bending [12]. Our device establishes uniform pure bending on a strand sample under large electromagnetic forces (Lorentz load) up to 3.6 kN/m, which were generated by the background magnetic field and the transport current of the test sample.

Bending tests were performed for five different Nb₃Sn wires developed by the ITER parties, using the pure bending device. Three of them were internal-tin wires of ITER TF US Oxford and Luvata wires and European (EU) EM-LMI wire, while two of them were EU European Advanced Superconductors (EAS) and Furukawa bronze wires. The critical currents were measured over a range of strains up to a nominal bending strain at the wire surface of 0.8%. Irreversible degradations of the critical currents due to bending were also evaluated.

An integrated model that accounts for neutral axis shift, current transfer length, mechanical filament breakage and uniaxial strain release due to the applied bending load has been developed recently. The pure bending experimental results have been analyzed with the integrated model.

In this paper we summarize in detail the design of the pure bending device and the test results of critical currents for ITER Nb₃Sn wires with the model analysis of Nb₃Sn wire results.

2. Versatile robust pure-bending device

2.1 Pure bending requirement

Conceptually, pure bending requires the bending of a sample into a circular arc of a uniform radius of curvature. This transformation process is illustrated in figure 1 where an initially straight beam is bent through a series of pure bending states.

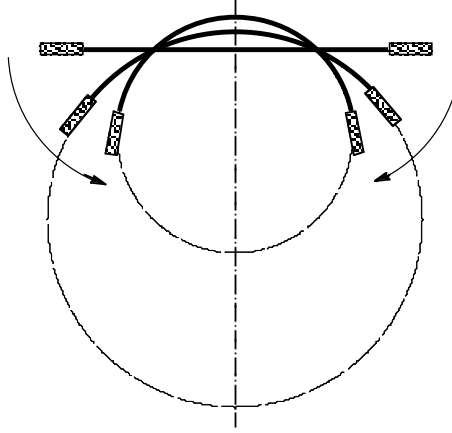


Figure 1. Evolution of a beam through pure bending states.

The coupling between the rotation of the ends of the beam and the horizontal movement can be found by solving a set of generalized constitutive beam equations originally presented by Simo [13] and applied to a large displacement pure bending device by Zineb, et al. [14]. These governing expressions, given by equations (1)-(3), relate the displacement of a beam to the internal normal force N , the shear V , and the moment distribution M , while allowing for large transformations.

$$N = \langle EA \rangle \left[\left(1 + \frac{du}{d\xi} \right) \cos \psi + \frac{dv}{d\xi} \sin \psi - 1 \right] \quad (\text{Normal force}) \quad (1)$$

$$V = \langle GA \rangle \left[\frac{dv}{d\xi} \cos \psi - \left(1 + \frac{du}{d\xi} \right) \sin \psi \right] \quad (\text{Shearing force}) \quad (2)$$

$$M = \langle EI \rangle \frac{d\psi}{d\xi} \quad (\text{Moment Distribution}) \quad (3)$$

where E is the modulus of elasticity, G is the shear modulus of elasticity, I is the area moment of inertia about the bending plane, and A is the cross-sectional area of the beam. The terms $\langle EA \rangle$ and $\langle GA \rangle$ represent the tensile and shearing stiffness while $\langle EI \rangle$ is the bending stiffness of the cross-section. The equations are essentially one-dimensional because they are given only in terms of the local axial coordinate of the beam, ξ . The

variables u , v , and ψ respectively give the horizontal displacement, vertical displacement, and rotation of a local section of the beam relative to its original undeformed position, as shown in figure 2.

Rigid clamps are attached to the ends of a straight beam of length L_s , as shown in figure 2a. The clamps are not allowed to deform when they are used to apply a moment couple M to the beam. As the beam clamps are rotated an angle θ from their original orientation, the length of the beam L_s , remains constant as shown in figure 2b. Due to the beam's bending stiffness, the applied moment must be increased as the clamp rotation angle increases.

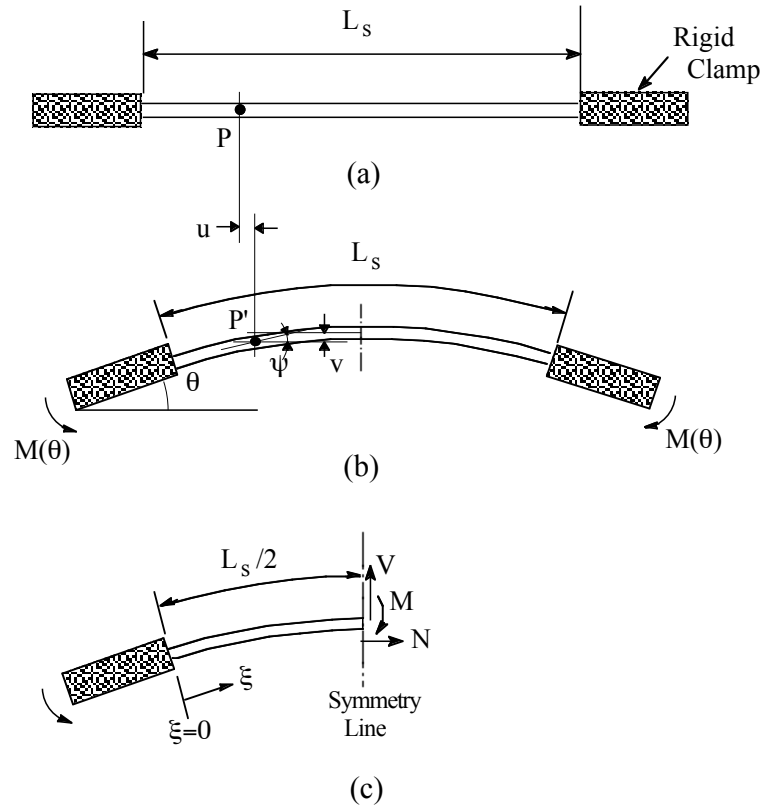


Figure 2. (a) Initially straight beam with rigid clamps, (b) Deformed beam, and (c) Half beam with symmetry.

Pure bending requires that the normal and shearing forces of the beam be zero and that the internal moment is constant [14], therefore

$$\left[\left(1 + \frac{du}{d\xi} \right) \cos\psi + \frac{dv}{d\xi} \sin\psi - 1 \right] = 0 \quad (4)$$

$$\left[\frac{dv}{d\xi} \cos\psi - \left(1 + \frac{du}{d\xi} \right) \sin\psi \right] = 0 \quad (5)$$

$$M = \langle EI \rangle \frac{d\psi}{d\xi} \quad (6)$$

Because the rotation of the beam at the local coordinate of $\xi = 0$ in figure 2c is equal to θ , and both the horizontal translation and rotation of the beam at the symmetry line must be zero for a pure bending state, the boundary conditions are given as follows;

$$\psi(\xi = 0) = \theta \quad (7)$$

$$u\left(\xi = \frac{L_s}{2}\right) = 0 \quad (8)$$

$$\psi\left(\xi = \frac{L_s}{2}\right) = 0 \quad (9)$$

Solving equations with the boundary conditions, one can obtain the horizontal translation as

$$u = \frac{1}{2} L_s \left[1 + \frac{1}{\theta} \sin \left[\theta \left(\frac{2}{L_s} \xi - 1 \right) \right] \right] - \xi \quad (10)$$

To produce pure bending, the required horizontal displacement at the coordinates of the beam at $\xi=0$ and $\xi=L_s$ from equation (10) can be given with the rotation θ by

$$u = \pm \frac{1}{2} L_s \left[1 - \frac{\sin\theta}{\theta} \right] \quad \begin{cases} + \text{ for } \xi = 0 \\ - \text{ for } \xi = L_s \end{cases} \quad (11)$$

The longitudinal bending strain ε_b at any section is given at the distance from the neutral axis, η by [14],

$$\varepsilon_b = -\eta \frac{d\psi}{d\xi} = \frac{2\eta\theta}{L_s} \quad (12)$$

The bending strain state is in tension at locations where η is positive (at the outside of the arc) and in compression where η is negative (at the inside of the arc). The bending strain is proportional to θ/L_s .

2.2 Pure bending device

It is relatively complex to make a mechanical device which produces precisely the nonlinear translation-rotation motion given by equation (10). In order to produce a good approximation to pure bending motion required by equations (11), we have adopted the lever-arm approach used by Goldacker *et al.* for testing high temperature superconductors [12]. The mechanism based on this method cannot produce the rotation-translation relationship of equation (10) required for pure bending over a large range of strain states, however it provides a way to design a robust and versatile pure-bending device which minimizes the deviation from the ideal bending of equation (10) for the strain states of interest.

The basic mechanism of a fabricated pure-bending device is illustrated in figure 3. The components consist of two rigid beam clamps attached at the ends of the beam. These clamps are connected to lever arms that rotate about a fixed pivot axis. The rigid lever arms in figure 3 are simply rotated so that the two ends of the beam move closer together and it is forced to assume the shape of a circular arc. The distance between two rotation axes is represented by L_p and the length of the beam is L_s . The lever arm length r can be chosen to minimize the amount of pure bending errors over a specific range of bending, since the lever arm length L_s is fixed during operation. This simple mechanical geometry can be analyzed to determine how well its movement correlates to that required to produce pure bending in the sample and estimate the amount of error that is introduced.

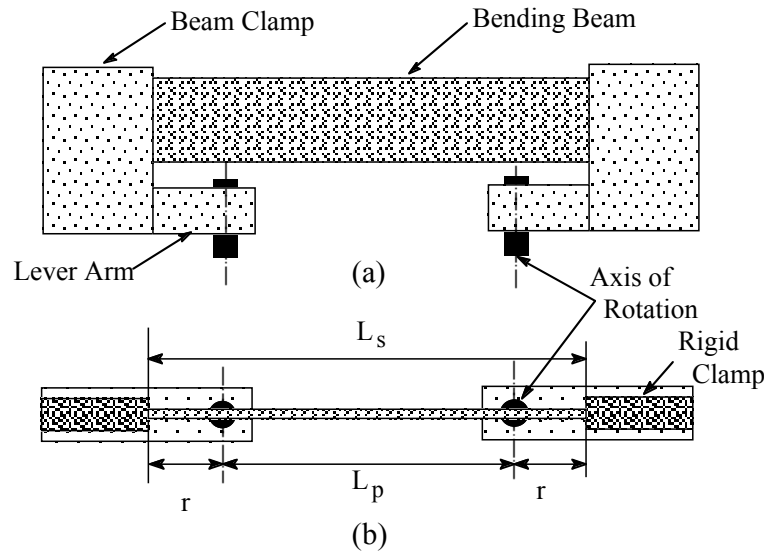


Figure 3. Bending mechanism geometry. (a) Side view of circular-type bending mechanism, and (b) Top view of circular-type bending mechanism.

Bending error minimization

Optimizing the mechanism to create quasi-pure bending in the beam consists of comparing the motion created by the lever arms to that required by the pure bending relationship. It is sufficient to do the optimization using equation (11) and an expression for the displacement-rotation caused by the lever arm motion.

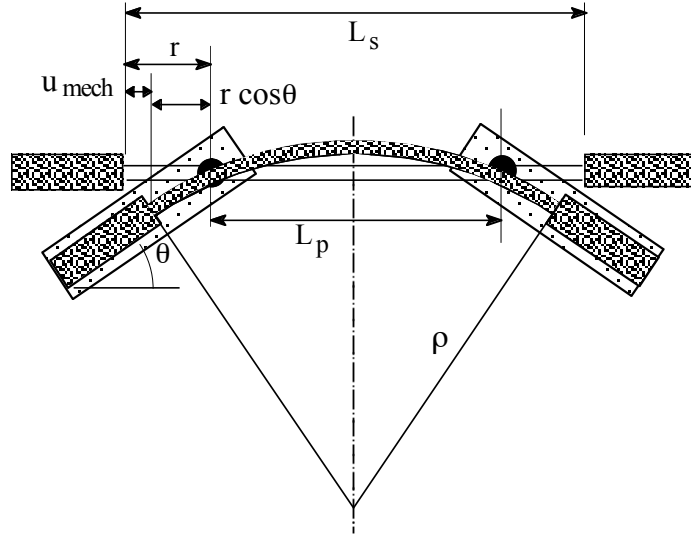


Figure 4. Initially straight sample bent into a circular arc.

As the lever arms of the mechanism are rotated an angle θ from the initial position in figure 4, the horizontal distance from the pivot axis to the beam ends, u_{mech} , is given by equation (13).

$$u_{mech} = r - r \cos \theta \quad (13)$$

where

$$r = (L_s - L_p) / 2 \quad (14)$$

The nondimensional expression of the horizontal displacement u_{mech} normalized by L_s is given as

$$\bar{u}_{mech} = (1 - f^{-1})(1 - \cos \theta) / 2 \quad (15)$$

here, defining f as done by Goldacker *et al.* [12] as the ratio of L_s to L_p

$$f = L_s / L_p \quad (16)$$

The ideal horizontal displacement required for pure bending, \bar{u}_{ideal} normalized by L_s is written from equation (11) as

$$\bar{u}_{ideal} = \frac{1}{2} \left[1 - \frac{\sin \theta}{\theta} \right] \quad (17)$$

To optimize the mechanism as close as possible to a pure bending condition, the error expression will be defined as the difference in the horizontal displacement between the ideal bending and the approximate bending mechanism as

$$\bar{u}_{error} \equiv \bar{u}_{ideal} - \bar{u}_{mech} \quad (18)$$

Substituting equations (15) and (17) into (18) results in

$$\bar{u}_{error} = \frac{1}{2} \left[\cos \theta - \frac{\sin \theta}{\theta} + \frac{1}{f} (1 - \cos \theta) \right] \quad (19)$$

Equation (19) could be plotted for many different values of the constant f to find the optimum geometry of the bending mechanism with the minimum error over a specified range of lever arm rotations, but a little math will help to quickly narrow down the possibilities. This is done by requiring the horizontal displacements to be equal at some angle of rotation and solving for f . Setting equation (15) equal to (17) and solving for f results in equation (20).

From equation (19), the error is a function of f and θ . The condition of the zero error is obtained by

$$f = \frac{1 - \cos \theta}{\frac{\sin \theta}{\theta} - \cos \theta} \quad (\theta \neq 0) \quad (20)$$

The f values are plotted as a function of the rotation angle θ in figure 5. The bending error could be minimized if the $f = L_s/L_p$ can be changed with the rotation angle θ according to equation (20) by adjusting the length L_p .

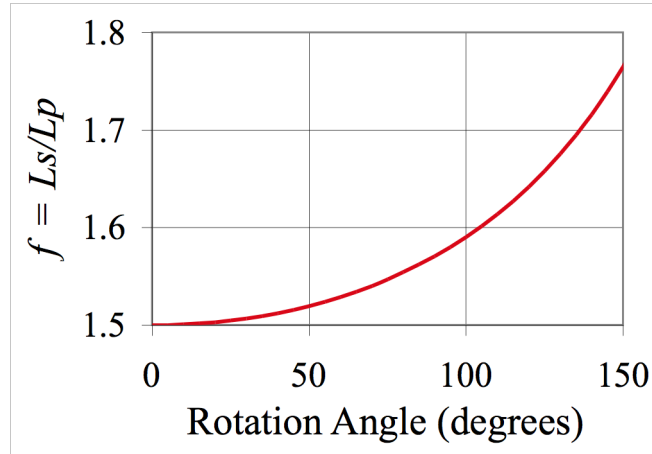


Figure 5. The f values given the error $\bar{u}_{error} = 0$ as a function of the rotation angle.

In reality, however, in the device shown in figure 3 the f value is constant since L_p is fixed. The f value must be designed to provide minimum bending error over a wide range of lever arm rotations. Figure 6 shows the errors of equation (19) for values of f ranging from 1.50 to 1.60 over the angles θ of zero to 120 degrees. Over the ranges of angular rotation up to 90 degrees the value $f = 1.55$ has the least average error. Up to the rotation of 56 degrees the value $f = 1.53$ has the least overall error. Consequently, this value of f will be used as the basis for designing the present bending device.

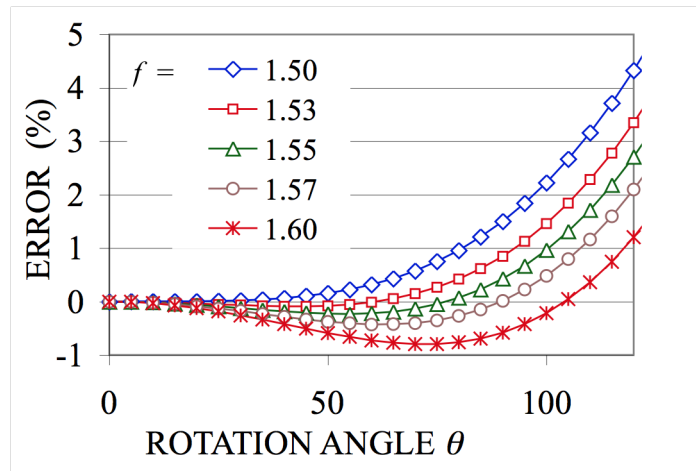


Figure 6. Plot of bending displacement errors as a function of the rotation angle.

Figure 6 shows that at low rotation angles (i.e. small displacements) the mechanism produces motion that is very close to ideal pure bending. But as the rotation angle increases

(i.e. large displacements) the design selection of f becomes important for minimizing the translation error.

It is important to note that the above error analysis does not provide a sense of how close to pure-bending strain the device would create in actual operation. In order to precisely evaluate pure bending errors, the governing constitutive equations (1)-(3) could be numerically solved with the appropriate boundary conditions to find the internal moment distribution, or a finite element analysis could be used.

3. Fabricated pure-bending test device for superconducting wire

3.1 Gear driving

The bending mechanism device shown in figure 7 was designed and constructed based on the principles discussed above. The overall diameter of the device was optimized to fit the 195 mm bore 20 T Bitter resistive 20 MW DC magnet at the National High Magnetic Field Laboratory (NHMFL) in Tallahassee, FL. The inclusion of the liquid helium cryostat reduced the available working bore size to 170mm.

The bending mechanism was driven by a gear system as shown in figure 7(a). A long shaft extending from outside of the cryostat to access the gears was connected to a small vertical worm-gear. The shaft was driven by a ½ horsepower motor. The vertical worm-gear drove a small horizontal worm-gear. This worm-gear was on the same shaft as a larger worm that rotated two larger worm-gears in opposite directions. These worm-gears served as the pivot axes for the bending motion and were connected to the lever arms that held the rigid beam clamps and the sample support beams, as seen in figure 7(b).

The bending beam-clamp mechanism was designed to hold two separated sample-holder beams as seen in figure 7(b). Each beam had two channel grooves machined into the upper and lower edges. Two beams provided the ability to test four samples simultaneously. Two different lever arm and beam systems were constructed corresponding to values of $f = 1.53$ and $f = 1.57$ for testing bending strains at the surface of a wire of about 0.82 mm diameter from 0% to 0.7% and from 0% to 0.9%, respectively.

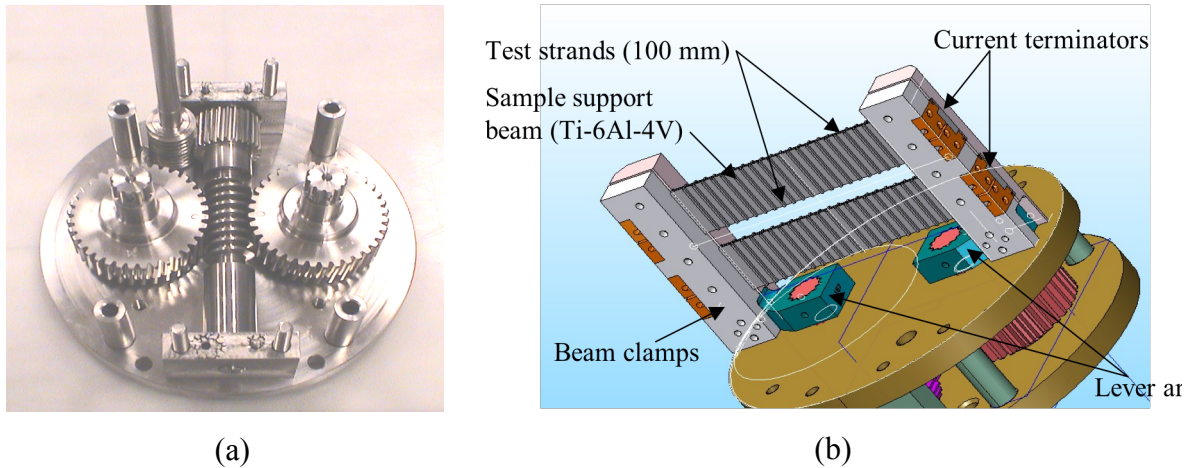


Figure 7. Pure-bending device. (a) Gear assembly. (b) Two sample holder beams mounted on the gear box. Each bending beam has two test strands on the upper and lower edges.

All of the structural components except the sample holder beams were constructed with 316 stainless steel. A single material was used so that the precise dimensional relationships between the components would remain constant from the room temperature assembly down to the liquid helium testing environment. Graphite (Graphokote[®] 83, Dixon) film coating was used to lubricate the moving parts and prevent the stainless steel from galling.

3.2 Sample holder beam

The sample holder beams were made from Ti-6Al-4V titanium alloy in the annealed condition. This material was chosen because its high elastic strain limit at liquid helium temperatures allowed a stiff support beam to be used while enabling the sample to be tested up to large bending strains. The published elastic strain limit of annealed Ti-6Al-4V at 4.2 K was found to be 1.4% [15].

An actual sample holder beam assembly is shown in figure 8. The assembly included two sample holder beams mounted between beam clamps, which are further illustrated by figure 7(b). Each sample holder beam could support two test samples that were mounted in grooved slots located at the top and bottom edges of each beam, as shown in figure 8(c). The beam plate dimensions were 26.1 mm x 165.4 mm x 4.06 mm (1.026" x 6.510" x 0.160"). The sample holder located the test wire at the neutral plane of the sample holder beam to maintain pure bending in the test sample wires. To restrict the maximum elastic

strain of the Ti-6Al-4V, the bending holder thickness was 1.68 mm (0.067"). In order to reinforce the thin wall of the sample groove areas against the Lorentz load, support ribs of 1.02 mm (0.04") width and 1.19 mm (0.047") thickness were machined vertically as shown in figure 8(c).

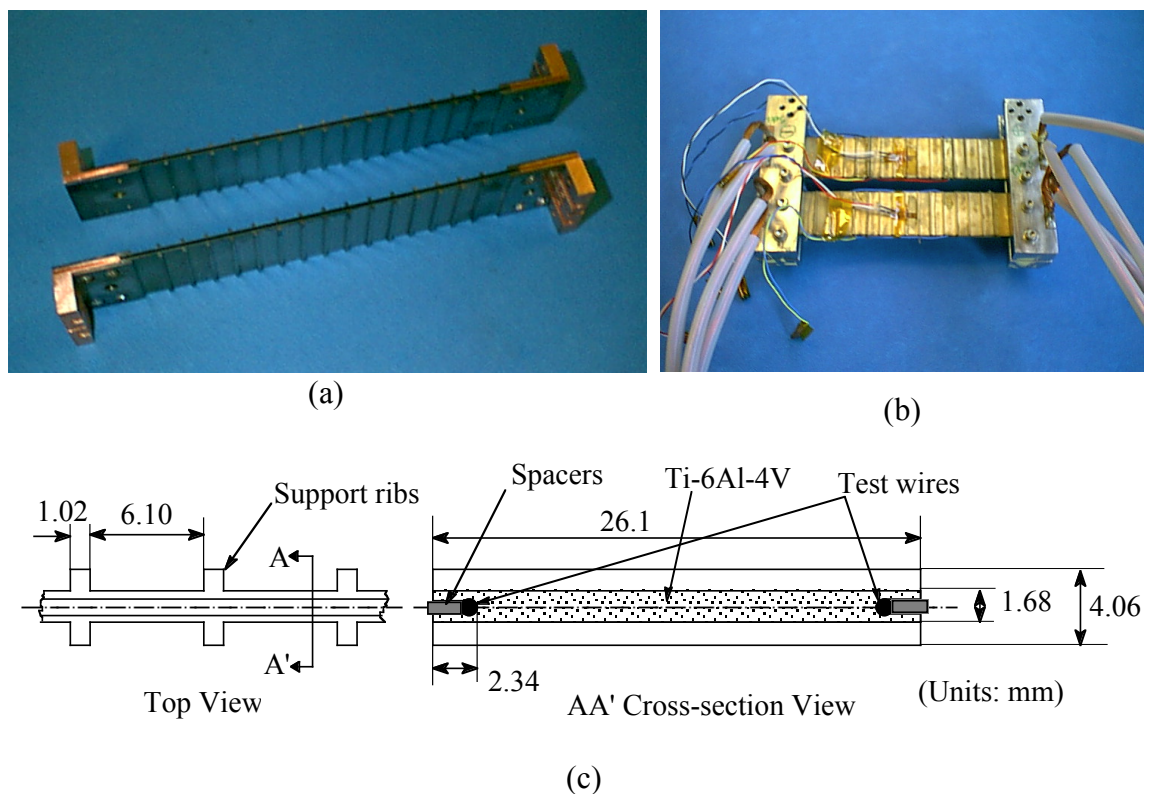


Figure 8. (a) Pure bending sample holders with copper terminations, (b) Sample assembly of two beams on the beam clamps with current leads and strain gauges. (c) Top and side cross-section views of the bending beam with the support ribs.

Two copper terminations were mounted at each end of the sample holder beam. The test wires were mounted on the beam before heat treatment. The grooves on the sample holder were fabricated for a snug-fit of the test wire. It is known that the diameters of Nb₃Sn superconducting wires increase by a few percent after heat treatment. Therefore, the test wire was tightly secured in the groove during the experiment. Additionally, as shown in figure 8(c), spacers made of stainless steel wires in the grooves secured the test samples. The spacers were fixed with stainless steel wires wrapped around the beam. All of the contact surface areas of the Ti-6Al-4V sample holder beam, including the test wires and the copper terminators, were coated with graphite film (Graphokote[®] 83) before assembly in

order to prevent sintering during heat treatment and to improve electrical insulation for testing.

Both ends of the test sample, 25 mm long, were soldered to the copper terminations (see figure 8(a) on the beam after heat treatment. Each sample had a pair of voltage taps. The voltage tap separation was 50 mm and the distance between a voltage tap and the copper termination was 25 mm. Figure 8(b) shows a sample holder assembly of two beams mounted on the beam clamps. A current lead was soldered to each copper termination.

The maximum bending strain of the test wire occurs at the greatest distance from the neutral axis (the sample's centerline) and the maximum bending strain $\varepsilon_{b \max}$ is given from equation (12) as a function of the rotation angle, by substituting in the wire diameter D .

$$\varepsilon_{b \max} = D \theta / L_s \quad (21)$$

The bending strain at other locations in the sample is linearly proportional to the distance from the neutral axis, and the strain state is in tension at the outside of the arc and in compression at the inside of the arc.

3.3 Effect of electromagnetic forces

Characterizing the critical current behavior of a superconducting wire sample in a background magnetic field creates an electromagnetic Lorentz force that affects the strain state of the sample. This is problematic for a pure bending test where the sample is suspended between the two loading clamps. It is then necessary to support the test sample with a beam that is sufficiently stiff so that it is not appreciably distorted by the electromagnetic forces, but flexible enough so that it can still be bent by the mechanism. For this approach, the test sample is placed in a channel machined into the edge of the support beam and the beam is directly bent by the motion of the mechanism clamps, rather than the sample itself, as described above. The beam channel thus serves as a template and guides the sample so that it assumes the same radius of curvature as the beam. Since the beam is not distorted by the Lorentz load, the test sample will not be distorted by it as well.

The test sample is not physically attached to the support beam channel except at the ends where it is connected to the electrical joints and the mechanism clamps. The beam channel

is machined in such a way so that the bending neutral axis of the sample coincides with the bending neutral axis of the beam. This arrangement allows the sample to assume the same bending profile as the beam without introducing additional undesired strains.

During critical current testing, both the sample and the beam are influenced by the electromagnetic forces, which push the sample into the side of the support beam channel. Analysis showed that the crushing effect of the electromagnetic force on the sample had little influence on the overall strain state of the sample, however the side load did tend to distort the bending curvature of the beam. As would be expected, this distortion was less significant with a stiffer support beam and finite element analysis was used to quantify the effect.

3.4 Finite element analysis

Finite element analysis (FEM) was used to verify the analytical predictions, study the influence of the electromagnetic forces, and refine the design of the bending device by considering details such as fillets and other machined features. Detailed treatments of the FEM analysis for the pure bending beams can be found in reference [8].

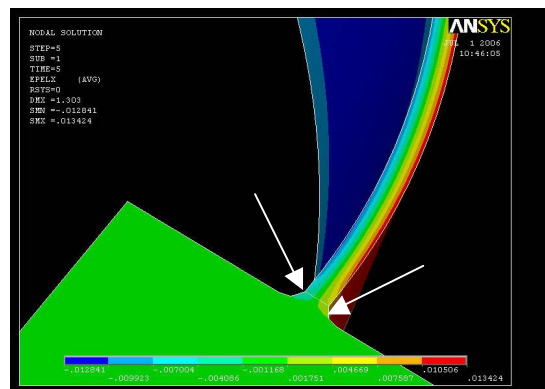


Figure 9. FEA analysis showing uniformity of the longitudinal strain (along the beam) with the strand sitting on the neutral axis (light green central plane). The rounding of the ends (shown by arrows) helps avoid stress concentration.

Figure 9 shows one of FEA analysis results of uniformity of the longitudinal strain (along the beam) with the strand sitting on the neutral axis (green central plane). The

rounding of the ends helps avoid stress concentration. The analysis showed that a bending radius of 1.19 mm (0.047”) at the joint of the beam to the support arm prevented unnecessary load concentration.

The FEA analysis supported the analytical predictions for the bending motion. It was able to show that for a properly optimized beam in the absence of electromagnetic forces the bending strain error introduced by the mechanism would be very small and the strain would remain within 10% of the ideal pure bending value for the worse case conditions at the ends of the beam length of 162.4 mm (6.392”). The strain would remain within 3% of the ideal pure bending value in the voltage-tap area over 50 mm at the center of the beam for worse case conditions.

It was confirmed that the support ribs on the bending beam effectively supported the Lorentz load, and did not affect the performance of pure bending beam. As shown in figure 10, FEA analysis showed uniformity of the bending with the strand sitting on the neutral axis (light green central plane). The beam shows variation of the longitudinal strain (x direction) in the y direction (perpendicular to the test wire), but maintains a neutral pure bending state in the center where the wire axis is located. The rib dimensions and the separations were optimized from FEA as shown in figure 8 (c).

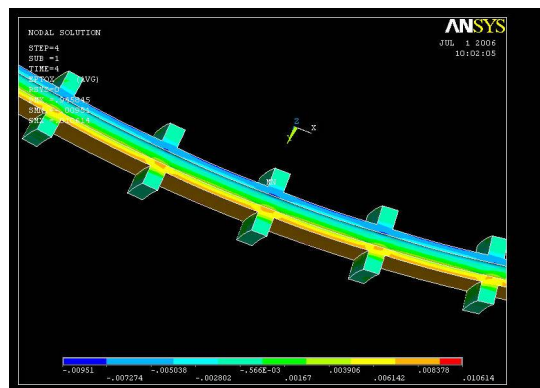


Figure 10. FEA analysis showing uniformity of the bending with the strand sitting on the neutral axis (light green central plane). The beam shows variation of the longitudinal strain (x direction) in the y direction but maintains a neutral pure bending state in the center where the wire is located.

The influence of the electromagnetic force on strain states of the beam was shown through both analytical and FEA analysis to be lower for stiffer beams and to decrease as the bending increased. When the beam is in the straight condition the only force in the

system is the electromagnetic load, which consequently dictates the strain state in the beam. The strain caused by the Lorentz load (for example 300 A at 12 T) in the straight state without bending is less than 0.035%.

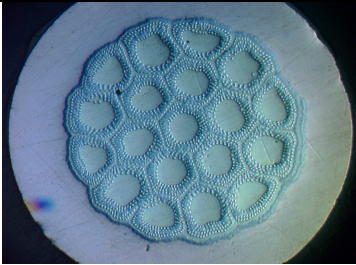
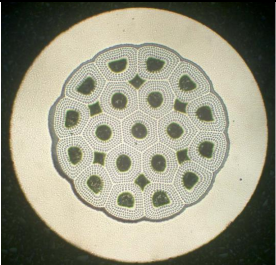
As the bending state of the beam increases, the internal moments in the beam begin to dominate and the electromagnetic force becomes a less significant contributor to the overall strain state. The contribution of the electromagnetic forces quickly becomes less important as the applied bending is increased. A secondary effect is that the critical current of the sample is lower at higher strains and this helps to further limit the influence of the electromagnetic force. For our beam design, the influence of the electromagnetic force was shown through FEA analysis to be negligible beyond the nominal bending strain of 0.3%.

4. Tested wires and critical current test conditions

Pure bending tests were performed for five different Nb₃Sn wires which were developed by the ITER parties. Three of them were internal-tin wires of ITER US TF pre-production Oxford and Luvata wires, and EU EM-LMI wire developed after ITER model coil tests in early 2000s. Two of them were bronze wires of EU EAS and Japanese Furukawa designs, developed for ITER model coils during the ITER Engineering Design Activity of the 1990's. Wire characteristics and their heat-treatment schedules are shown in tables 1 and 2.

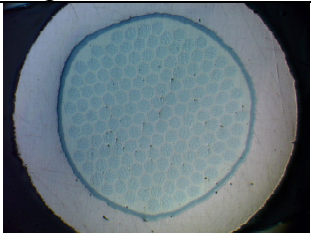
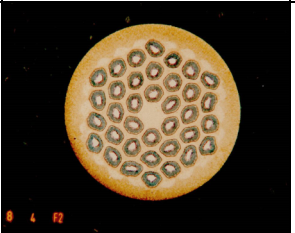
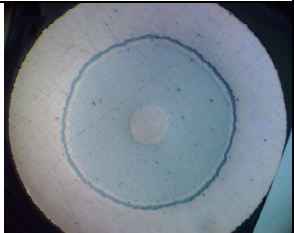
The critical currents were measured with the voltage criterion of $E_c=100 \mu\text{V/m}$ at every 0.1% nominal bending strain up to 0.8%. Irreversible degradation of the critical current was measured by releasing bending after each 0.1% strain increment. All tests were performed using the 20 T, 195 mm Bitter magnet at NHMFL, Florida State University. In the next section, typical test results of each wire are shown. More detailed data can be found in [10]. The pure bending beam used in the testing was designed for a bending strain up to 0.7% with a 0.82 mm wire sample diameter, based on the elastic limit of the Ti-6Al-4V beam material. However, the beam was used up to 0.8% bending strain slightly above the limit.

Table 1. ITER US TF Pre-production Oxford and Luvata wires.

Strand Manufacturer	Oxford	Luvata
Wire ID	B9355-2BE	NT8404
Technique	Internal tin	Internal tin
Strand Diameter (mm)*	0.817	0.818
Cu : non-Cu*	1.076	1.075
Twist pitch (mm)*	10	13
Heat treatment	Ramp up to 210 °C with 10 °C/h and hold for 50 hours, ramp up to 340 °C with 10 °C/h and hold for 25 hours, ramp up to 450 °C with 10 °C/h and hold for 25 hours, ramp up to 575 °C with 10 °C/h and hold for 100 hours, ramp up to 650 °C with 10 °C/h and hold for 200 hours.	Ramp up to 200°C with 10°C/h and hold for 50 hours, ramp up to 460°C with 15°C/h and hold for 50 hours, ramp up to 575°C with 50°C/h and hold for 100 hours, ramp up to 650°C with 50°C/h and hold for 175 hours, and Ramp down at 25°C/h.
Cross section		 Courtesy of Tae Pyon, Luvata.

* Manufacturer's data

Table 2. ITER related EU and Japanese wires. The EM-LMI and Furukawa wires are from the ITER model coil program.

Strand Manufacturer	EU EAS	EU EM-LMI	Japanese Furukawa
Wire ID	NSTT8305-HK002-A2	Wire used for BM3	SG-96071-08
Technique	Bronze	Internal tin	Bronze
Strand Diameter (mm)*	0.806	0.806	0.809
Cu : non-Cu*	0.92	1.38	1.58
Twist pitch (mm)*	15	9.9	17.9
Heat Treatment	Ramp up to 205 °C with 10 °C/h, ramp up to 210 °C with 5 °C/h and hold for 50 hours, ramp up to 340 °C with 10 °C/h and hold for 25 hours, ramp up to 450 °C with 10 °C/h and hold for 25 hours, ramp up to 575 °C with 10 °C/h and hold for 100 hours, ramp up to 660 °C with 10 °C/h and hold for 100 hours, and ramp down at 25 °C/h.	Ramp up to 120°C with 20°C/h, ramp up to 180°C with 68°C/h, ramp up to 200°C with 20°C/h and hold for 50 hours, ramp up to 340°C with 68°C/h and hold for 24 hours, ramp up to 650°C with 68°C/h and hold for 200 hours, and ramp down at 73°C/h.	Ramp up to 650 °C with 50 °C/h and hold for 240 hours, and ramp down at 20 °C/h.
Cross Section		 Courtesy of A. Nijhuis, Univ. of Twente.	

* Manufacturer's data

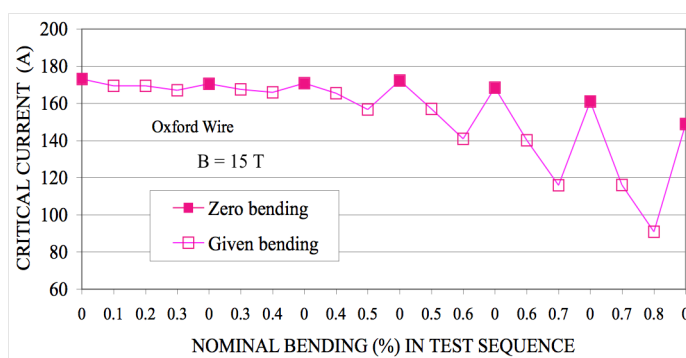
The bending strain values mentioned above, for example 0.8%, are so called nominal values of the maximum bending strain at the wire surface. The actual peak bending strain of the filaments of the tested wires was less than the nominal bending strain values. The ratio of the peak bending strain to the nominal bending strain depends on the Cu:non-Cu ratio of the wire, scaling as the ratio of the strand diameter to that of the non-copper area. In the

case of the Oxford and Luvata wires, 0.8% nominal bending corresponds to about 0.55% peak filament bending strain.

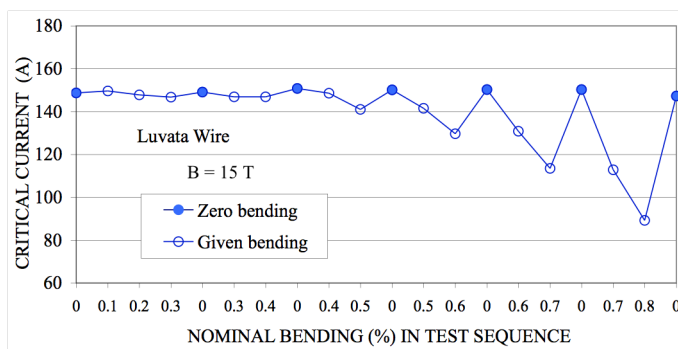
5. Test Results

5.1 ITER TF pre-production Oxford and Luvata wires

Test results of the critical currents of Oxford and Luvata wires at 15 T are plotted for the nominal bending strains in Figure 11 (a) and (b), respectively. The x-axis of each figure is the nominal bending strains applied in the order of the test sequences.



(a)



(b)

Figure 11. The critical currents of two Oxford wire samples are plotted for the nominal bending strains in the order of testing. (a) Oxford strand, and (b) Luvata strand.

As seen in figure 11 the critical currents degraded with increasing bending strains. At about 0.8% nominal bending strains (corresponding to about 0.55% peak filament bending) the critical currents were degraded by 47% from 173 A to 91 A for Oxford wire and by 40% from 149 A to 89 A for Luvata wire. The initial critical currents of the Oxford wire was much higher than that of the Luvata wire, however at 0.8% bending the Oxford and Luvata

wires resulted in similar critical currents. Irreversible degradations of Oxford and Luvata wires after the 0.8% nominal bending were about 13% and 1.3%, respectively. It is noted that there is a significant difference of the bending effect between those two wires, even though both wires were made by internal tin Nb₃Sn process to identical specifications.

A typical motor (½ horsepower) speed for ramping up and down the bending test corresponded to about 0.0015% of the nominal bending rate per second for a 0.8 mm diameter wire. At the end of the series bending tests, a quick ramp test was performed in liquid helium. When the ramping speed was increased to 0.0046% per second, which was three times faster than the normal test speed, one of the sample holder beams was broken just before reaching 0.8% bending, as shown in Figure 12.

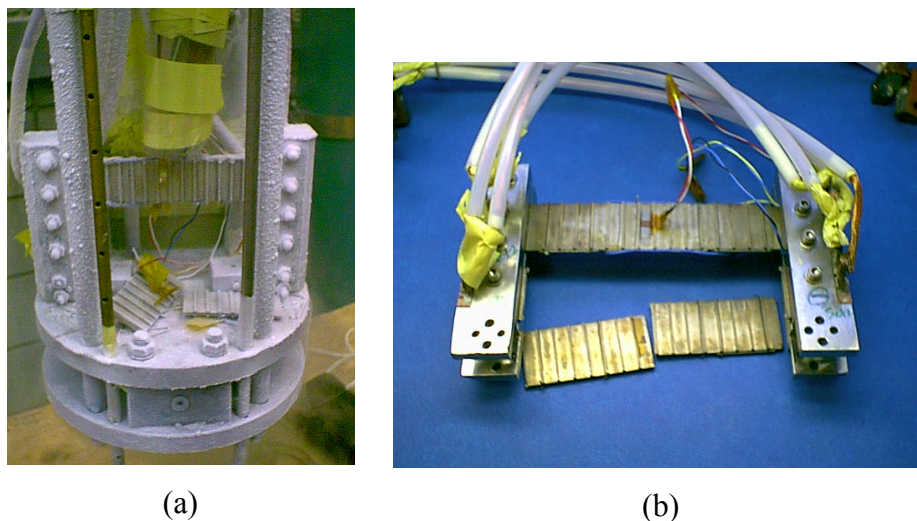


Figure 12. One of the pure bending beams was broken just before reaching 0.8% bending when the bending was applied at the fast rate of 0.0046% per second, which was three times faster than the normal speed.

5.2 Other ITER-related wires

In the second series of bending tests, three wires, EU EAS, EM-LMI and Japanese Furukawa wires, were tested. These wires were tested in the same way as that used for the Oxford and Luvata wires, but the magnetic field strength for the bending tests of these samples was 12 T instead of 15 T.

5.2.1 EU EAS wire

The critical currents measured with various bending at 12 T are plotted with the nominal bending strains in test sequence in figure 13. The critical current of the EAS sample degraded by 12% from 205 A to 180 A at 0.8% nominal bending (corresponding to about 0.58% peak filament bending) strains. Permanent degradation was about 2%.

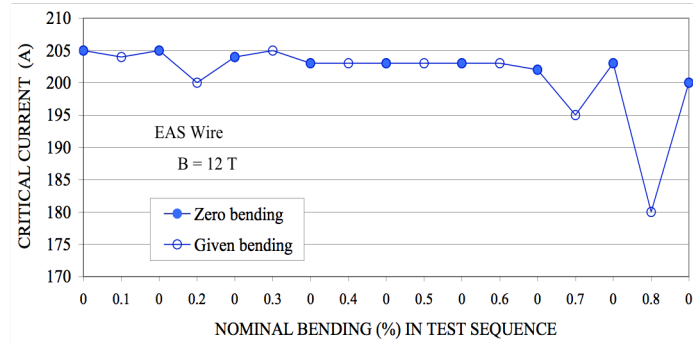


Figure 13. The critical currents of two EAS wire samples are plotted for the nominal bending strains in the order of testing.

5.2.2 EM-LMI wire (ITER model coil wire)

The critical currents of the sample measured at 12 T are plotted with the nominal bending strains in the test sequence in figure 14. The critical current of EM-LMI samples degraded by about 23% from 160 A to 124 A at the 0.8% nominal bending (corresponding to about 0.52% peak filament bending) strains. However, it was noticed for the EM-LMI samples that the critical currents did not show permanent degradation.

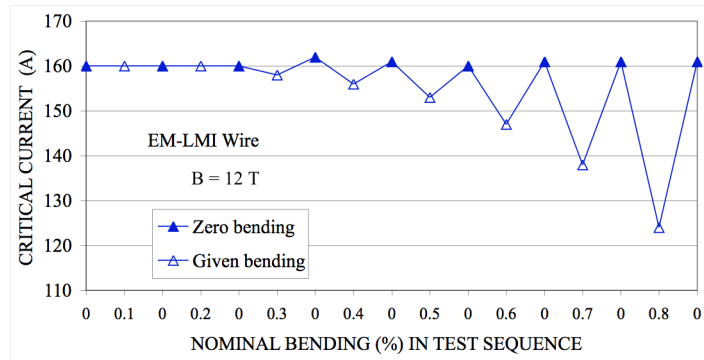


Figure 14. The critical currents of EM-LMI wire sample are plotted for the nominal bending strains in the order of testing.

5.2.3 Furukawa wire (ITER model coil wire)

The critical currents measured at 12 T are plotted with the nominal bending strains in the order of testing in figure 15. The critical currents of the Furukawa samples degraded by

12% from 154 A to 136 A at the 0.8% nominal bending (corresponding to about 0.50% peak filament bending) strains. The critical currents of the Furukawa samples at the zero bending strain increased gradually after each bending cycle. It was noticed for Furukawa samples that the critical currents increased by 1% at the peak bending strains of about 0.3%, and the critical current increased to 157 A after the bending cycles.

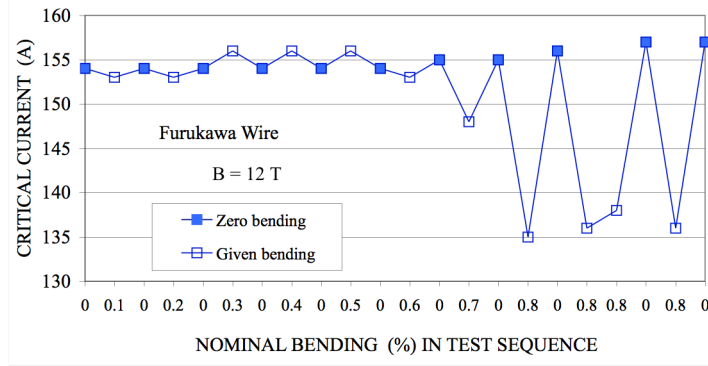


Figure 15. The critical currents of Furukawa wire are plotted for the nominal bending strains in the order of testing.

6. Model analysis

6.1 Critical current formula

The scaling formula for the critical current of Nb_3Sn wires was recently recommended (based on various researchers' works) by Bottura [16] and Devred [17]. To analyze the critical current of the bending effects, we followed the recommendation, but we used the fixed parameters of $p=0.5$ and $q=2$, which formula was originally proposed by Godeke, et al. [18].

The critical current density is given:

$$J_c = \frac{C}{B} s(\varepsilon)(1 - t^{1.52})(1 - t^2)b^p(1 - b)^q \quad (22)$$

The strain function:

$$s(\varepsilon) = 1 + \frac{1}{1 - C_{a1}\varepsilon_{0a}} \left[C_{a1}(\sqrt{\varepsilon_{sh}^2 + \varepsilon_{0a}^2} - \sqrt{(\varepsilon - \varepsilon_{sh})^2 + \varepsilon_{0a}^2}) - C_{a2}\varepsilon \right] \quad (23)$$

$$\varepsilon_{sh} = C_{a2}\varepsilon_{0a} / \sqrt{C_{a1}^2 - C_{a2}^2} \quad (24)$$

Critical temperature:

$$T_C^*(B, \varepsilon) = T_{C0\max}^* [s(\varepsilon)]^{\frac{1}{3}} (1 - b_0)^{\frac{1}{1.52}} \quad (25)$$

Critical field:

$$B_{C2}^*(T, \varepsilon) = B_{C20\max}^* s(\varepsilon) (1 - t^{1.52}) \quad (26)$$

Reduced magnetic field:

$$b = B / B_{C2}^*(T, \varepsilon) \quad (27)$$

Reduced magnetic field at zero temperature:

$$b_0 = B / B_{C2}^*(0, \varepsilon) \quad (28)$$

Reduced temperature:

$$t = T / T_C^*(0, \varepsilon) \quad (29)$$

C = The scaling constant

$B_{C20\max}^*$ = The upper critical field at zero temperature and strain

$T_{C0\max}^*$ = The critical temperature at zero field and strain

p = The low field exponent of the pinning force ($p < 1$, $p \approx 0.5$)

q = The high field exponent of the pinning force ($q \approx 2$)

C_{a1} = The strain fitting constant

C_{a2} = The strain fitting constant

ε_{0a} = The residual strain component

ε_{\max} = The tensile strain at which the maximum critical properties are reached.

6.2 Conventional model of bending effects on strand critical current

The critical current of a multi-filamentary superconducting strand under bending strain has been formulated by Ekin [19], and his concept has been adopted for various work [1], [20]-[22]. Ekin considered critical current distributions due to uniaxial strain geometry in twisted filaments of a strand under bending while taking into account the current transfer length between filaments with regards to the twist pitch length. Two extreme cases have been considered: long twist pitch (or low inter-filament resistivity), and short twist pitch (or high inter-filament resistivity). We will call the former case ‘‘Perfect Current Transfer,’’ and the latter ‘‘No Current Transfer.’’

6.2.1 Perfect Current Transfer

If currents can transfer between filaments without electric loss (zero transverse resistance), the critical current of a multifilamentary strand can be obtained from the total current of one cross-section of a strand [19]. The critical current of a strand is given by

$$I_c = 2 \int_{-R_{nc}}^{R_{nc}} j_c(\varepsilon_y) \sqrt{R_{nc}^2 - y^2} dy \quad (30)$$

$$\varepsilon_y = \varepsilon_0 + \varepsilon_{by} \quad (31)$$

$$\varepsilon_{by} = y/R_b \quad (32)$$

here,

R_{nc} = The radius of the non-copper area

ε_0 = The precompressive strain

6.2.2 No Current Transfer

If the transverse resistance between filaments is high enough and no current can transfer between filaments, the critical current of each filament can be limited by the worst point in one twist pitch with regard to bending strain distributions. Therefore, the current of a strand is given by [19]

$$I_c = 2\pi \int_0^{R_{nc}} j_c(\varepsilon_y) y dy \quad (33)$$

here,

$$\varepsilon_{by} = \begin{cases} -\frac{y}{R_b} & \text{for } j_c(\varepsilon_0 - \frac{y}{R_b}) < j_c(\varepsilon_0 + \frac{y}{R_b}) \\ +\frac{y}{R_b} & \text{for } j_c(\varepsilon_0 - \frac{y}{R_b}) > j_c(\varepsilon_0 + \frac{y}{R_b}) \end{cases} \quad (34)$$

Note that the worst point of the critical current does not occur always at the compression side. At a large bending rate the tension side may create larger degradation of the critical current than the compression side since the critical current decreases at the tension side more sharply than at the compression side. To account for this effect, we introduce a minimum function operator to express a minimum value of $j_c(\varepsilon)$ in the range of strains between $-\varepsilon_{by}$ and $+\varepsilon_{by}$. Using the minimum function operator, equation (33) can be rewritten as,

$$I_c = 2\pi \int_0^{R_{nc}} \left\{ \min |j_c(\varepsilon_y)|_{\varepsilon_y = \varepsilon_0 + \varepsilon_{by}}^{\varepsilon_y = \varepsilon_0 - \varepsilon_{by}} \right\} y dy \quad (35)$$

6.3 Integrated model

In general, it has been known that the experimental results of the critical currents under a wide range of bending strains fit neither the Perfect Current Transfer model nor the No Current Transfer model. Our experimental results were only a good fit to the Perfect Current Transfer model at small bending rates and then sharply drop off toward the prediction line of No Current Transfer model with increasing bending. We have investigated four effects due to mechanical bending [11]: the neutral-axis shift [19], [23], [24], the current transfer length, the filament breakage [25, 26], and the uniaxial strain releasing [23], [27].

6.3.1 Neutral-axis shift effect

A shift of the neutral-axis due to yielding of the strand matrix under bending has been pointed out by Ekin [19]. When the neutral-axis shifts toward the compressive side by δ as shown in figure 16, the bending strain ϵ_{by} is given by

$$\epsilon_{by} = \frac{y + \delta}{R_b - \delta} \quad (36)$$

The peak bending strain on the tension and compression sides are written respectively as,

$$\epsilon_{bp}^+ = \frac{R_{nc} + \delta}{R_b - \delta} \quad (37)$$

$$\epsilon_{bp}^- = -\frac{R_{nc} - \delta}{R_b - \delta} \quad (38)$$

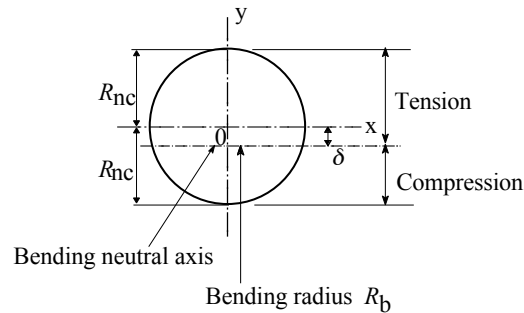


Figure 16. Cross-section of non-copper showing the neutral axis shift of δ .

The critical currents for Perfect Current Transfer and No Current Transfer can be obtained with equations (36)–(38) by equations (30) and (35), respectively. All integrations in this work were carried out by the Gaussian integration method of order 40 using Microsoft Excel[®].

Figures 17 and 18 show the calculated neutral-axis shift effect on the critical current for the Perfect Current Transfer and No Current Transfer cases, respectively. As seen here, there are significant differences between the Perfect Current Transfer and No Current Transfer cases. In the Perfect Current Transfer case the critical current shows a maximum peak at certain conditions of bending and neutral axis shift since the tension area increases. This was observed for the Furukawa wire (figure 28). However, in the No Current Transfer case there is no such peak, since the critical current is dominated by the worst point of the critical current.

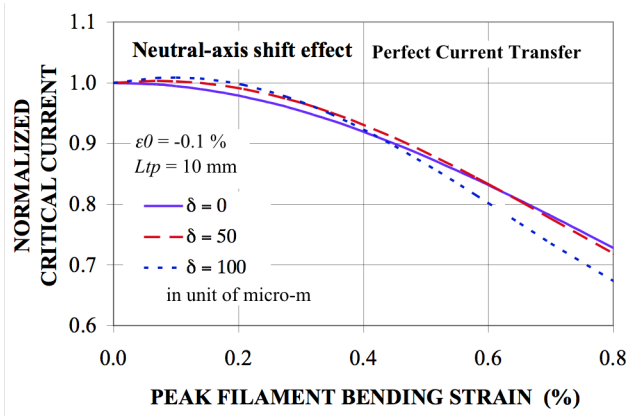


Figure 17. Calculated normalized critical currents of neutral-axis shift effect for Perfect Current Transfer.

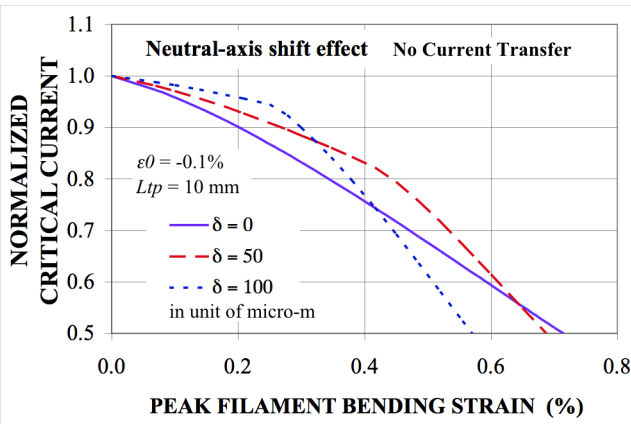


Figure 18. Calculated normalized critical currents of neutral-axis shift effect for No Current Transfer.

6.3.2 Current transfer length effect

As mentioned earlier, all trends of measured critical currents at various bending strains are between those of Perfect Current Transfer and No Current Transfer. The current transfer length affects the total critical currents with regard to the twist pitch length L_{tp} since the critical current changes periodically along a filament. Therefore the ratio of the current transfer length and the twist pitch, L_{ct} / L_{tp} , will be an important factor for critical current behavior. The current transfer length L_{ct} has been given as a function of the transverse resistance of matrix material between filaments and the n-value of the resistive transition of the superconductor by [21], [28], [29],

$$L_{ct} = d \sqrt{\frac{0.106}{n} \frac{\rho_m}{\rho^*}} \quad (39)$$

here,

n = The empirical power factor ($\rho = kJ^n$) representing the resistive transition in the superconductor

ρ_m = The transverse resistance of the matrix between filaments

ρ^* = The superconductor resistivity criterion of the critical current

d = The conductor diameter [28]. Reference 21 used the strand diameter for d ; however, the diameter d is a measure with regard to the current transfer spacing between filaments, therefore d could be much smaller than the strand diameter.

It is noted that regardless of the accuracy of the current transfer length itself, the relative ratio of the current transfer length to the twist pitch (L_{ct}/L_{tp}) is an important factor for characterizing the current transfer effects on the critical current. It should be emphasized that the current transfer length is a function of the n-value, as well as the transverse resistance.

To take into account the current transfer effect, the critical current of a filament at a given point z along a filament is assumed to be dominated by the minimum critical-current value between $z - L_{ct}/2$ and $z + L_{ct}/2$. Now the critical current can be given using the minimum function operator defined for equation (35) as in cylindrical coordinates,

$$I_c = 2 \int_0^{R_{nc}} \int_{-\frac{\pi}{2}}^{\frac{\pi}{2}} \left\{ \min_{\substack{\phi=\varphi+\varphi_{ct} \\ \phi=\varphi-\varphi_{ct}}} |j_c(\epsilon_{r\phi})| \right\} r d\varphi dr \quad (40)$$

$$\varepsilon_{r\phi} = \varepsilon_0 + \varepsilon_{br\phi} \quad (41)$$

$$\varepsilon_{br\phi} = \frac{r \sin \phi}{R_b} \quad (42)$$

$$\varphi_{ct} = \frac{2\pi L_{ct} \sin \theta}{L_{tp}} \quad (43)$$

$$\theta = \tan^{-1} \frac{L_{tp}}{2\pi R_{nc}} \quad (44)$$

where,

L_{ct} = The minimum current transfer length

L_{tp} = The twist pitch length of strand

Figure 19 shows the calculated critical currents as functions of current transfer length effects with various current transfer lengths L_{ct} of 0.5 mm, 1 mm, 2.5 mm and 5 mm for a strand with the twist pitch $L_{tp} = 10$ mm. These L_{ct} values correspond to 0, 5%, 10%, 25% and 50% of the twist pitch length. The curves of $L_{ct} = 0$ and $L_{ct} = 0.5 L_{tp}$ agree with the results of Perfect Current Transfer (open circles) and No Current Transfer (open triangles), respectively.

To apply the neutral-axis shift effect to the current transfer model, the strain equation (42) is replaced with the following equation,

$$\varepsilon_{br\phi} = \frac{r \sin \phi + \delta}{R_b - \delta} \quad (45)$$

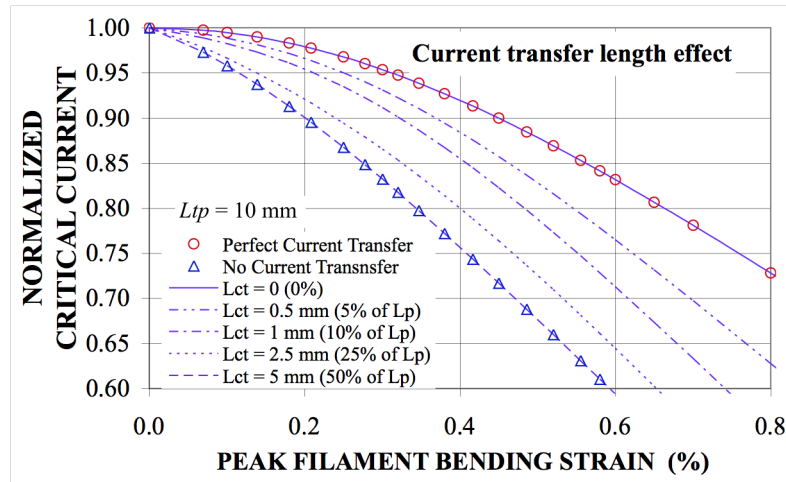


Figure 19. Calculated critical currents of current transfer effect with various current transfer length L_{ct} .

6.3.3 Filament breakage effect

Filament breakages in the tension side due to bending have been found [25], [26]. Such filament breakage is probably the dominant cause of the irreversible permanent degradation. If filament breakage occurs on the surface of the tension side as shown in figure 20, the critical currents can be obtained with integration over the unbroken area in the above-mentioned methods. Note that in the case of No Current Transfer the effective superconducting filaments are only in the center circular section which does not overlap the broken area, since the strand is twisted. Therefore degradations of the No Current Transfer case due to breakage are much more significant than those of the Perfect Current Transfer case.

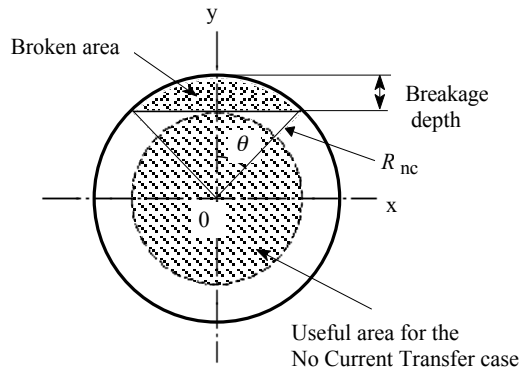


Figure 20. Schematic of non-copper area having broken filament area.

Figure 21 shows the calculated critical currents of the filament breakage for the Perfect Current Transfer and No Current Transfer cases with the breakage fractions of 0%, 2% and 5%. In the case of Perfect Current Transfer, critical current degradations are the same rates of the breakages. On the other hand the degradations of the No Current Transfer case are significant. For example, it is about 35% for the 5% breakage at zero bending, since the outer layer filaments in the annulus of the breakage depth pass the broken area in one twist pitch as illustrated in figure 20. The filament breakage effects of those cases on the critical currents are shown as a function of the breakage in figure 22. The relationship between the breakage fraction and the breakage depth is shown in figure 23. The 5% breakage

corresponds to the breakage depth of about 55 μm for the non-copper area diameter of 567 μm (10% of the non-copper diameter).

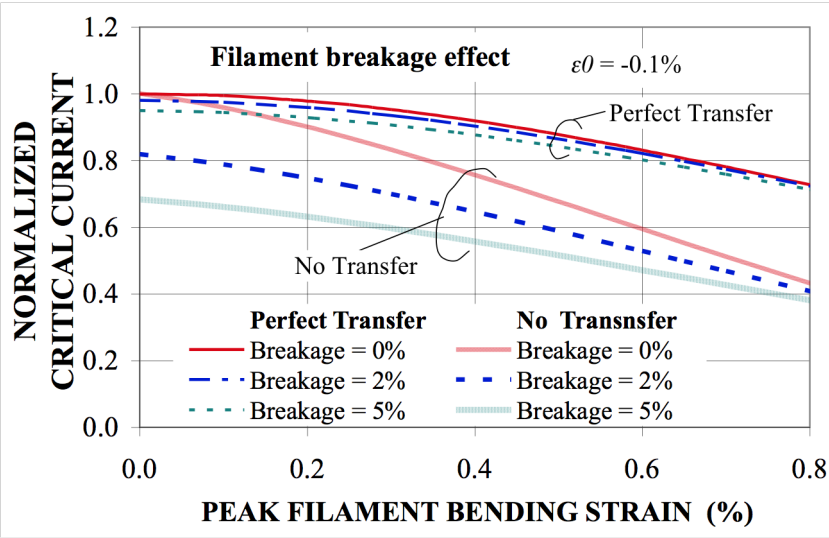


Figure 21. Calculated normalized critical currents of the filament breakage effect of the Perfect Current Transfer and No Current Transfer cases for the breakage fractions of 0%, 2% and 5%.

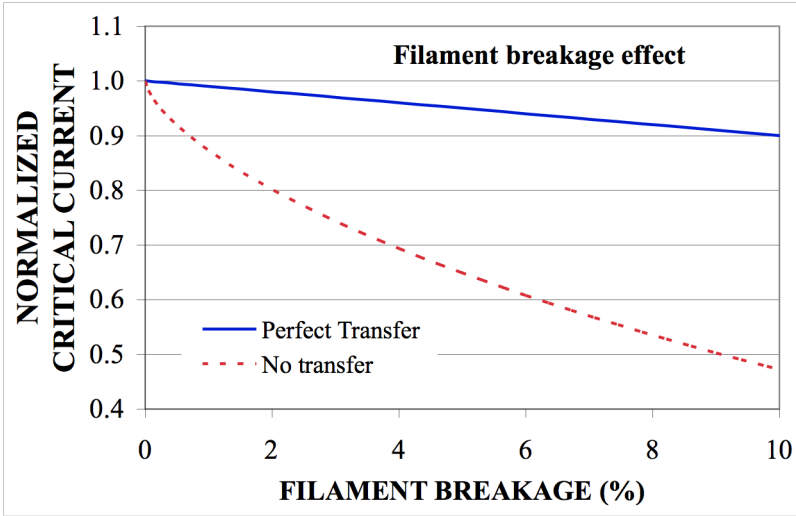


Figure 22. Filament breakage effects on the critical currents for Perfect Current Transfer (dark line) and No Current Transfer (dotted line) as a function of the breakage.

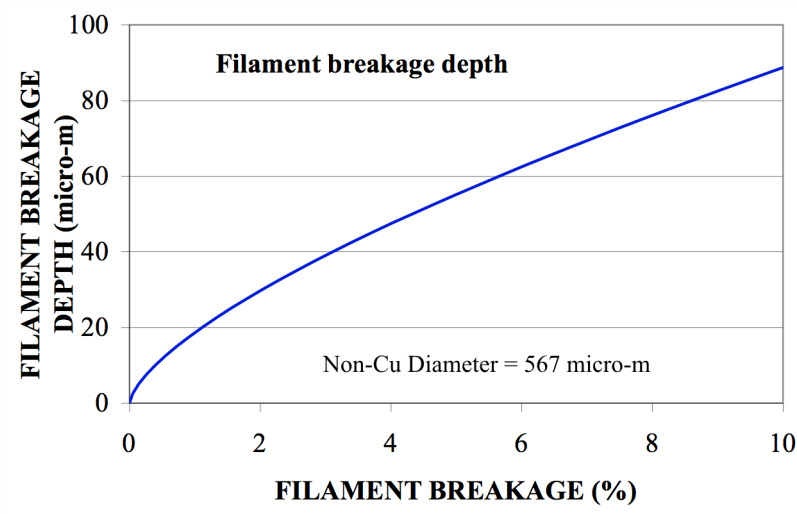


Figure 23. Breakage depth as a function of the breakage fraction.

6.3.4 Uniaxial strain release effect

Uniaxial thermally induced precompressive strain during cooldown after reaction of a Nb_3Sn wire could be released by mechanical bending cycles [27]. The result is that the strain $|\varepsilon_{max}|$ becomes smaller, and the critical current increases. The increase of the critical current at zero bending after bending cycles could be driven only by this strain release effect. In the present experiments, this effect seemed to be very small, but did happen for some wires.

7. Discussion

Pure bending behaviors of five different Nb_3Sn wires were examined. The critical current of each wire is different under bending strains. The neutral axis shift explains the increase of the critical currents at small bending strain before large degradations. The current transfer length expresses deviations of experimental results from Perfect and No Current Transfer Models. The filament breakage shows the irreversible permanent degradation after mechanical cycles of bending strains. The uniaxial strain release could explain the slight increase of the critical currents after bending cycles.

To use the scaling law of equation (22) for analyses of the experimental results, seven parameters of the equation were required. However there was no parameter study for the exact wires used here. Therefore, the parameters C_{a1} , C_{a2} , and ε_{oa} were obtained on the basis

of various published work of similar wires [16]-[18], [30]-[32]. Other parameters were adjusted by our measured critical current results of magnetic field dependences (12 T to 15 T). The parameters used for the tested wires are summarized in table 3. The parameters of p and q were 0.5 and 2, respectively.

Table 3. Scaling equation parameters used for curve fittings.

Strand	Oxford	Luvata	EAS	EM-LMI	Furukawa
B^*_{c20max} (T)	32.5	32.5	35.75	28.7	32.5
T^*_{c0max} (K)	17.8	17.0	16.52	16.89	16.5
C (AT)	18500	17000	14150	12750	11500
ϵ_{0a}	0.00344	0.0034	0.0025	0.0019	0.0020
ϵ_{max}	0.0005	0.0011	0.0024	0.0011	0.0023
C_{a1}	53.3	60.0	71.39	45.16	44.35
C_{a2}	8.55	20.0	28.28	8.45	12.25

Curve fitting results for the Oxford sample are shown in figure 24. Measured data lie between curves obtained from the Perfect Current Transfer model (upper thin line) and the No Current Transfer model (lower thin line). The bold line was obtained by curve-fitting taking account of the four effects: the neutral axis shift, the current transfer length, the filament breakage and the uniaxial strain release, in order to fit the experimental data. Each parameter of the four effects used for the fittings are shown as a function of the bending strain in figure 24. Three dotted purple lines in figure 24 show recovery curves of the critical currents after the peak bendings of 0.42%, 0.49% and 0.56%, respectively. The recovered critical currents at zero bending agree well with the experimental results. The Oxford wire sample showed significant irreversible permanent degradation, which could be explained with 2% filament breakage at 0.56% bending strain.

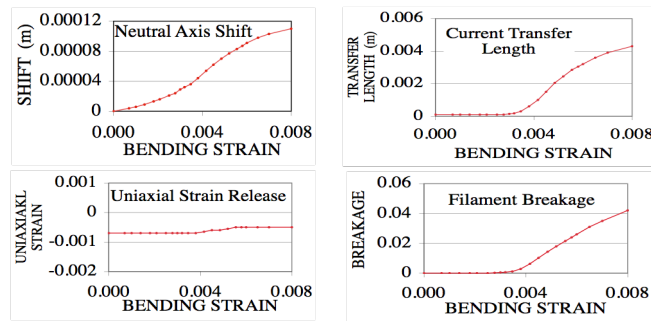
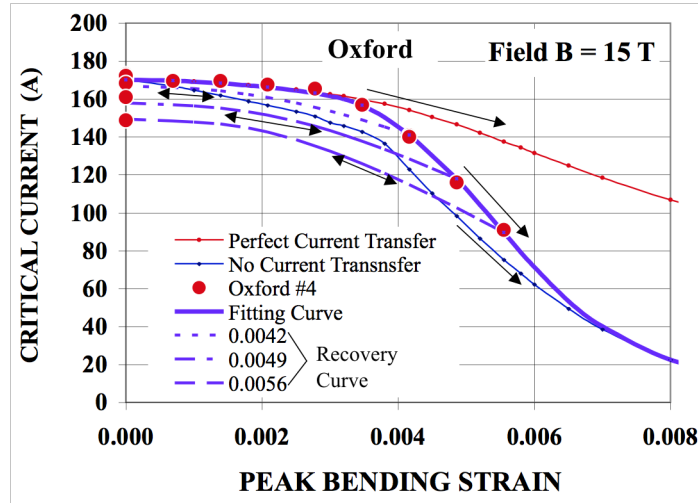


Figure 24. Curve fittings (top large figure) of the critical currents measured for Oxford wire (solid circles). Lines are obtained from model calculations using estimated behaviors of the neutral axis shift, the current transfer length, the breakage and the uniaxial strain release (four lower small figures): Upper thin and lower thin lines are for Perfect Current Transfer and No Current Transfer models, respectively. Measured results fit a bold line which was obtained from the newly developed model.

Figure 25 shows the curve fitting results of a Luvata wire sample, which were obtained with the four effects shown in the figure. The sharp decrease of the critical current above 0.45% bendings was reflected by the sharp increase of the current transfer length. Permanent degradation of the Luvata sample was negligible, implying an absence of filament breakage.

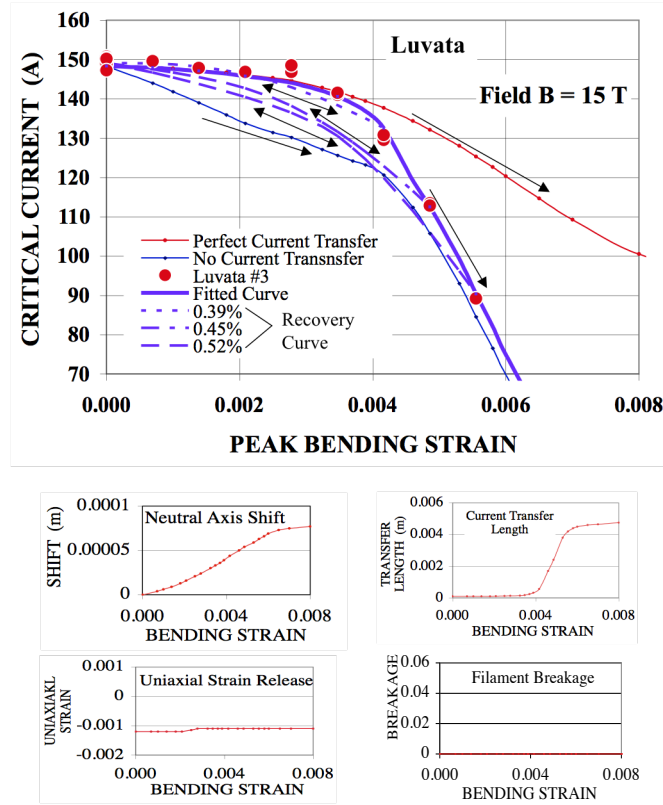


Figure 25. As in figure 24, but for Luvata wire.

Figure 26 shows the curve fitting results of an EU EAS wire sample, which were obtained with the four effects. The performance of the EAS wire sample was affected relatively little by the bending strain. The critical current increases slightly with increasing bending strains. This probably is the result of neutral axis shifts.

Figure 27 shows the curve fitting results of an EU EM-LMI wire sample, which were obtained with the four effects shown in the figure. The internal tin EM-LMI sample showed bending effects as large as other internal tin wires of Oxford and Luvata wires. Permanent degradation of this wire was small, similar to the Luvata wire.

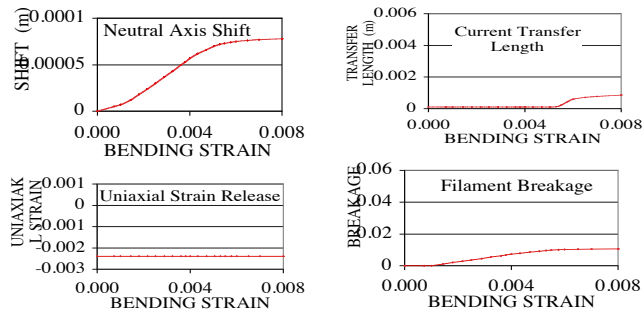
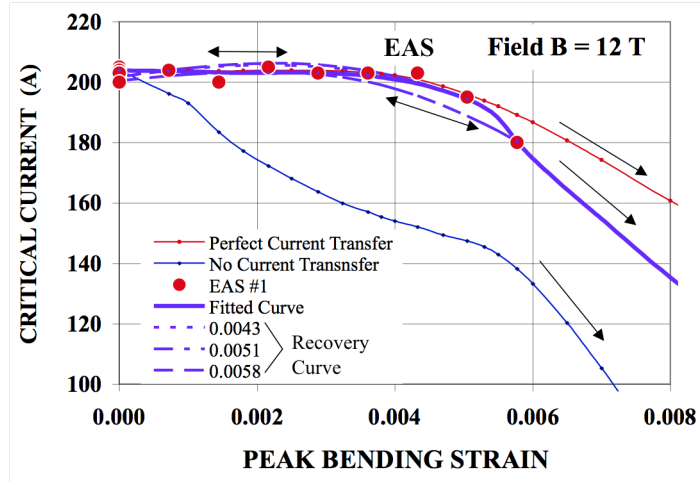


Figure 26. As in figure 24, but for EU EAS wire.

Figure 28 shows the curve fitting results of a Furukawa wire sample, which were obtained with the four effects shown in the figure. The 1% increase of the critical current for the Furukawa wire sample at 0.3% peak bending can be simulated by assuming a 70 μm shift of the neutral axis.

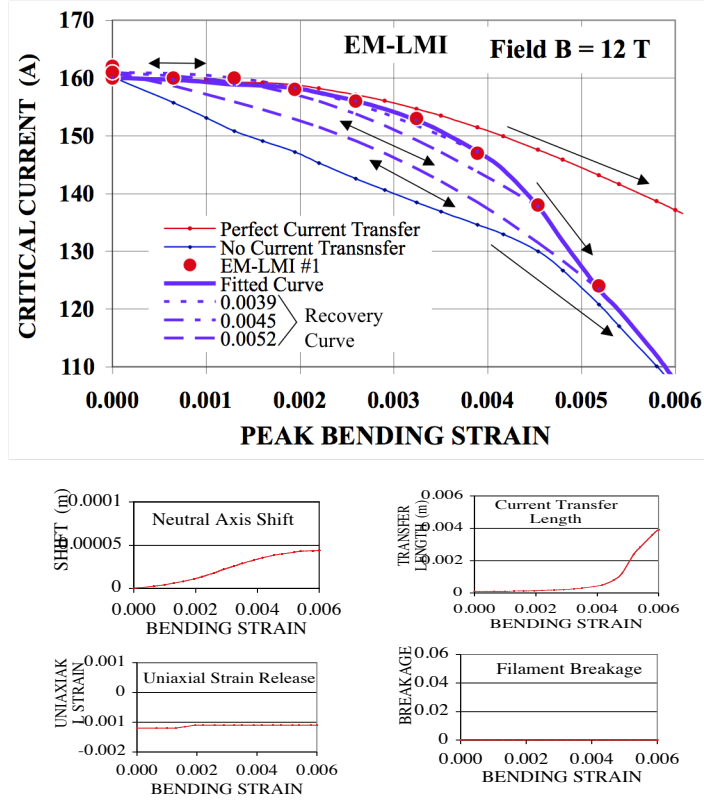


Figure 27. As in figure 24, but for EU EM-LMI wire.

The current transfer lengths obtained from data fittings are plotted as a function of the square root of the n -values in figure 29. The EAS results were not included in this figure since the data were very limited. It has been found that the current transfer length L_{ct} has a linear relationship with $1/\sqrt{n}$, even though L_{ct} is not exactly proportional to $1/\sqrt{n}$ as it is predicted from equation (39) [23],

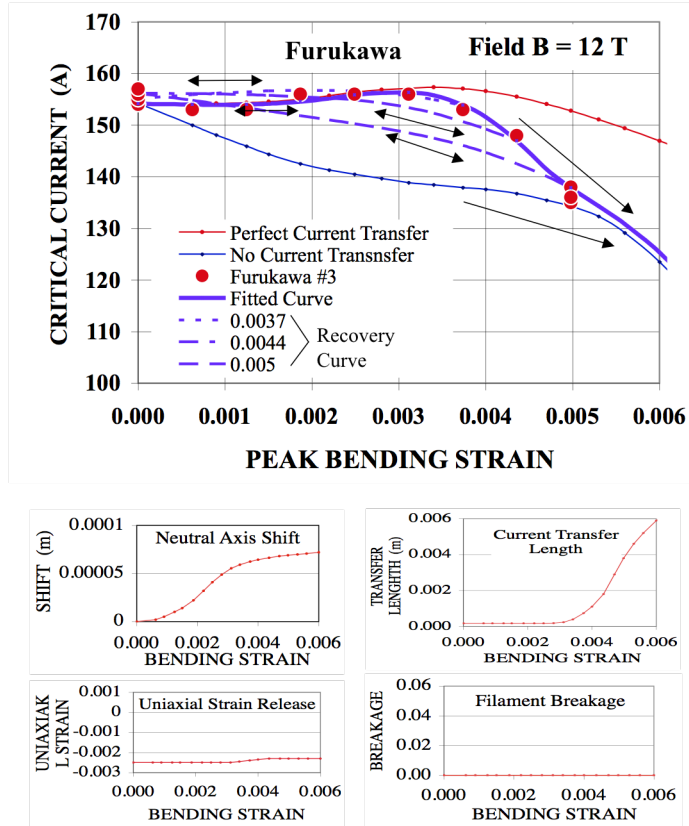


Figure 28. As in figure 24, but for Furukawa wire.

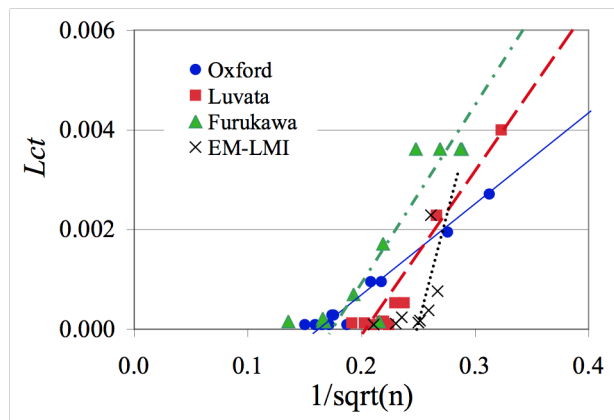


Figure 29. Current transfer lengths L_{ct} obtained from data fittings as a function of square root of n -values.

Each of four effects; the neutral axis shift, the current transfer length, the filament breakage and the uniaxial strain release, had a very different contribution to the critical

currents, respectively, so that their four fitting parameters were relatively easy to determine. However, the resulted parameters for the five samples might not be definitive determinations.

The calculated neutral axis shifts, for all of the samples, were quite large. Further investigations of the mechanical dynamics of the superconducting matrixes during bending are recommended. The recovery behavior of the critical currents after applying bending is especially useful for understanding the effects of bending on the critical currents.

8. Conclusions

A robust pure-bending test device for characterizing the critical currents of high performance superconducting strands has been developed. The test samples were placed along the midline of the edges of a support beam plate made of Ti-6Al-4V, which was bent through an evolution of pure bending states without axial tension and compression. This pure-bending test device was able to apply variable uniform bending strains up to 0.9% in a liquid helium environment on a strand sample that was subject to large electromagnetic forces due to the background magnetic field and the transport current. The bending strain characteristics and the irreversibility behaviors of ITER high performance Nb₃Sn strands were tested under variable bending strains up to 0.8%.

The critical currents of the internal tin wires were degraded at 0.8% nominal bending strain by 47% for Oxford wire, 40% for Luvata wire and 30% for EM-LMI wires. Higher current density wire, such as the Oxford wire, seems to degrade more than lower current density wires. On the other hand with the 0.8% nominal bending, bronze wires of Furukawa and EAS both degraded only by 10%. After 0.8% nominal bending, Oxford, Luvata and EAS wires showed 13%, 1.3% and 2% irreversible permanent degradation of their initial critical current values, respectively. However, the critical currents of EM-LMI and Furukawa wires were gradually increased at zero bending strain after each bending cycle. It was found that the Furukawa wire showed clear improvements of the critical currents at the peak bendings of around 0.3%.

The experimental behaviors of the critical currents due to pure bending have been evaluated with the four effects: the neutral axis shift, the current transfer length, the filament breakage and the uniaxial strain release. The neutral axis shift increases the critical current

under small bending strains ($\sim 0.3\%$), but does not change the critical current at zero bending state. The current transfer length reduces the critical current with regard to the ratio of the current transfer length and the twist pitch length. The current transfer length effect seems to be an important factor, which is a function of the n-value of the superconductor and the transverse resistance of the matrix. A strand having a longer twist pitch has a smaller effect due to the current transfer length. Longer strand twist pitch is desired for bending reasons, although it is typically harmful for AC coupling losses. The filament breakage reflects an irreversible permanent degradation. The filament breakage could result in significant degradation for a strand having a long current transfer length (short twist pitch). The uniaxial strain release (reduction of thermally induced strain) enhances the critical current.

Better understanding of the bending behavior of Nb₃Sn wires has been obtained by using a newly developed integrated model that accounts for neutral axis shift, current transfer length, mechanical filament breakage and uniaxial strain release. However, further investigations of both electrical and mechanical properties of superconducting wires under pure bending are required.

Acknowledgements

The authors would like to thank A. Nijhuis at University of Twente, T. Isono at JAEA and A. Vostner at EFDA for providing the Nb₃Sn wires used for this work, and Joel Schultz for stimulating this work. This work was supported by the U.S. Department of Energy and the US ITER Project Office. A portion of this work was performed at the National High Magnetic Field Laboratory, Florida State University, which is supported by NSF and DOE.

References

- [1] N. Mitchell, "Mechanical and magnetic load effects in Nb₃Sn cable-in-conduit conductors," *Cryogenics*, vol. 43, 2003, pp. 255–270.
- [2] N. Martovetsky, "ITER model coil tests overview: Nb₃Sn strand properties in cable-in-conduit conductors," *Physica C*, 401, 1, pp 22-27, 2004.
- [3] Y. Nunoya, T. Isono, and K. Okuno, "Experimental investigation on the effect of transverse electromagnetic force on the V-T curve of the CIC conductor," *IEEE Trans. Appl. Supercond.* 14, 1468-1472, 2004.
- [4] A. Nijhuis and Y. Ilyin, W. Abbas, B. ten Haken, and H.H.J. ten Kate, "Performance of an ITER CSI model coil conductor under transverse cyclic loading up to 40000 cycles," *IEEE Trans. Appl. Supercond.* 14, 1489-1494, 2004.

- [5] N. Mitchell, "Operating strain effects in Nb₃Sn cable-in-conduit conductors," *Supercond. Sci. Technol.*, vol. 18, 2005, pp. 396–404.
- [6] Y. Zhai and M.D. Bird, "Florida electro-mechanical cable model of Nb₃Sn CICC for high-field magnet design," *Supercond. Sci. Technol.* **21** (2008) 115010 pp. 1-15.
- [7] D.L. Harris, "Characterization of Nb₃Sn superconducting strand under pure bending," MIT Mechanical Engineering Masters Thesis, 2005.
- [8] A. Allegritti, "Development and experimental test of a device for the measurements of the critical current of superconducting strands under pure bending conditions," University of Bologna, Department of Mechanical Engineering, Italy, 2006.
- [9] D.L. Harris, A. Allegritti, M. Takayasu, and J.V. Minervini, "Pure bending strand test of high performance Nb₃Sn wires," *Adv. Cryo. Eng.*, 54, Plenum, N.Y., 341-348, 2008.
- [10] M. Takayasu, L. Chiesa, J.H. Schultz, and J.V. Minervini, "Bending-strain test results of ITER Nb₃Sn wires and preliminary model analysis," MIT PSFC report, PSFC/JA-08-41, July 2008.
- [11] M. Takayasu, L. Chiesa, J.H. Schultz, and J.V. Minervini, "Bending effects on critical currents of Nb₃Sn superconducting wires," *Adv. Cryo. Eng.*, 56, Plenum, N.Y., 239-246, 2010.
- [12] W. Goldacker, S.I. Schlachter, R. Nast, H. Reiner, S. Zimmer, H. Kiesel, and A. Nyilas, "Bending strain investigation on BSCCO(2223) tapes at 77K applying a new bending technique," *Advances in Cryogenic Engineering*, 48, 469-476, 2002.
- [13] J.C. Simo, K.D. Hjelmstad, and R.L. Taylor, "Numerical formulations of elastoviscoplastic response of beams accounting for the effect of shear," *Computer methods in applied mechanics and engineering*, 42, 301-330, 1984.
- [14] T.B. Zineba, A. Sedrakianb, J.L. Billoetb, "An original pure bending device with large displacements and rotations for static and fatigue tests of composite structures," *Composites part B: Engineering*, 34, 447-458, 2003.
- [15] W.F. Brown, H. Mindlin, C.Y. Ho, *Aerospace Structural Materials Handbook*, CINDA/USAF CRDA Handbooks Operation, Purdue University, 1993.
- [16] L. Bottura, 2.4.2008, "Jc(B,T,ε) Parameterization for ITER Nb₃Sn Production," CERN-ITER collaboration report, Version 2, April 2, 2008.
- [17] A. Dervred, "ITER Nb₃Sn critical surface parameterization," ITER Organization memo, October 4, 2008.
- [18] A. Godeke, B ten Haken, H.H.J. ten Kate, and D.C. Larbalestier, "A general scaling relation for the critical current density in Nb₃Sn," *Supercond Sci Technol*, 19, R100-R116, 2006.
- [19] J.W. Ekin, "Strain Scaling law and the prediction of uniaxial and bending strain effects in multifilamentary superconductors," in *Filamentary A15 Superconductors*, Proceedings of the tropical conference on A15 superconductors, Ed by M. Suenaga and A. Clark, Plenum Press, New York, 187-203, 1980.
- [20] A. Nijhuis and Y. Ilyin, "transverse load optimization in Nb₃Sn CICC design; influence of cabling, void fraction and strand stiffness," *Supercon. Sci. Technol.* 19, 945-962, 2006.
- [21] A. Nijhuis, Y. Ilyin, W.A.J. Wessel and W. Abbas, "Critical current and strand stiffness of three types of Nb₃Sn strand subjected to spatial periodic bending," *Supercon. Sci. Technol.* 19, 1136-1145, 2006.

- [22] N. Koizumi, Y. Nunoya, and K. Okuno, "A new model to simulate critical current degradation of a large CICC by taking into account strand bending," *IEEE Trans. Appl. Supercond.* 16, 831-834, 2006.
- [23] K. Kaiho, T.S. Luhman, M. Suenaga, W.B. Sampson, "Effects of bending on the superconducting critical current density of monofilamentary Nb₃Sn wires," *Appl. Phys. Lett.* 36, 223-225, 1980.
- [24] Y. Kubo and T. Ozawa, "Derivation of I_c degradation rate for reacted Nb₃Sn wires under applied bending and tensile strains," *Cryogenic Engineering, Journal of the Cryogenic Society of Japan in Japanese*, 37, 68-76, 2002.
- [25] M.C. Jewell, P.J. Lee and D.C. Larbalestier, "The influence of Nb₃Sn strand geometry on filament breakage under bend strain as revealed by metallography," *Supercond Sci Technol*, 16, 1005-1011, 2003.
- [26] B.J. Senkowicz, M. Takayasu, P.J. Lee, J.V. Minervini, and D.C. Larbalestier, "Effects of Bending on Cracking and critical Current of Nb₃Sn ITER wires," *IEEE Trans. Appl. Supercond.* 15, 3470-3473, 2005.
- [27] K. Miyoshi, S. Awaji, H. Oguro, G. Nishijima, and K. Watanabe, "I_c enhancement effect in Nb₃Sn Coils fabricated by the react-and-wind method," *Adv. Cryo. Eng.*, 52, Plenum, N.Y., 536-543, 2006.
- [28] J.W. Ekin, "Current transfer in multifilamentary superconductors. I. Theory," *J. Appl. phys.* 49, 3406-3409, 1978.
- [29] J.W. Ekin, A.F. Clark, and J.C. Ho "Current transfer in multifilamentary superconductors. II. Experimental results," *J. Appl. phys.* 49, 3410-3412, 1978.
- [30] A. Nijhuis, "A solution for transverse load degradation in ITER Nb₃Sn CICC: verification of cabling effect on Lorentz force response," *Supercond Sci Technol*, 21, 1-15, 054011, 2008.
- [31] Y. Ilyin, A. Nijhuis and E. Krooshoop, "Scaling law for the strain dependence of the critical current in an advanced ITER Nb₃Sn strand," *Supercond. Sci. Technol.* 20, 186-191, 2007.
- [32] D.M.J. Taylor and D.P. Hampshire, "The scaling law for the strain dependence of the critical current density in Nb₃Sn superconducting wires," *Supercond. Sci. Technol.* 18, S241-S252, 2005.